

# A Novel Range-Instantaneous-Doppler ISAR Imaging Algorithm for Maneuvering Targets via Adaptive Doppler Spectrum Extraction

Lijie Fan\*, Si Shi, Yang Liu, Shiyu Xu, and Zengping Chen

**Abstract**—A novel range-instantaneous-Doppler (RID) algorithm of inverse synthetic aperture radar (ISAR) imaging based on adaptive Doppler spectrum extraction is proposed in this paper. Regarding maneuvering targets, such as military aircraft, the ISAR image is blurred on cross-range domain when the range-Doppler (RD) algorithm is applied. The RID imaging method is often used to resolve the Doppler ambiguity but there are some scattering points that could be lost because the sliced time is fixed in traditional RID imaging. To the method proposed in this paper, the optimal Doppler spectrum of each range bin is extracted by gradient energy function (GEF) after time-frequency (TF) analysis and then all of the optimal Doppler spectrums are combined to obtain a final 2-D RID image of the target. Compared with the traditional RID method, the novel algorithm can obtain image with better focused quality. The results obtained from simulated and field-measured data verify the superiority of the proposed algorithm.

## 1. INTRODUCTION

Inverse synthetic aperture radar (ISAR) imaging can generate high resolution 2-D images for non-cooperative targets and is of great value in military applications [1–4]. Range resolution is proportional to the bandwidth of transmitted signal whilst cross-range resolution is dependent on the relative rotation of targets with respect to the radar. For maneuvering targets, such as military aircraft, the rotation in coherent processing interval (CPI) is nonuniform. The Doppler frequency shifts are time varying. Thus, the ISAR image is blurred on cross-range domain when the range-Doppler (RD) algorithm is applied [5].

Range instantaneous Doppler (RID) imaging is often used to resolve the Doppler ambiguity caused by non-uniform rotation [6]. The major difference between RD and RID methods is that time-frequency (TF) analysis is used in RID imaging while Fourier transform (FT) is used in RD imaging. The instantaneous ISAR image of the target can be obtained by taking the slices in the slow-time domain [7–13]. In general, the traditional RID methods take the same time slice for all range bins. In that case, some 2-D scattering points of the target may disappear in instantaneous ISAR image, because the TF energy distribution of different range bins along the slow time is not definitely constant. In practice, when the sample time in slow-time domain is fixed, the instantaneous Doppler spectrums of each range bin will not always contain all of the scattering points in the azimuth direction. That will be proved by simulation in Section 3.

Aiming at these problems, a new RID ISAR imaging method based on adaptive Doppler spectrum extraction (ADSE) is proposed. In this algorithm, the optimal instantaneous Doppler spectrum of each range bin is extracted automatically by using the gradient energy function (GEF), which is introduced in Section 4. Then, the Doppler spectrum with the maximum gradient energy is selected as the instantaneous image of each range bin. A final RID image of the target is obtained by combining these optimal instantaneous images. Experimental results obtained from simulated and field-measured

---

*Received 25 December 2014, Accepted 13 February 2015, Scheduled 19 February 2015*

\* Corresponding author: Lijie Fan (jackson\_akg@163.com).

The authors are with the Science and Technology on Automatic Target Recognition Laboratory, National University of Defense Technology, Changsha 410073, China.

data show that the image of the improved RID technique is better focused and more holonomic than those obtained using the traditional methods.

The remainder of this paper is organized as follows. In Section 2, the rotational ISAR imaging model of maneuvering targets is constructed. Section 3 describes the traditional RID imaging algorithm. A simulated analysis of its shortcoming is also discussed. The novel RID imaging algorithm by ADSE is detailed in Section 4. In this section, the ADSE evaluation function is described. Experimental results and performance analysis are reported in Section 5, followed by conclusions in Section 6.

## 2. ROTATIONAL ISAR IMAGING MODEL FOR MANEUVERING TARGET

In this section, we construct the rotational ISAR imaging model for maneuvering targets. A simple geometry of ISAR imaging is shown in Figure 1. The instantaneous distance from the scattering point  $p(x_p, y_p)$  to the radar can be approximated as [14]:

$$R_p(t) \approx R_0 + y_p \cos \theta(t) + x_p \sin \theta(t) \quad (1)$$

where  $R_0$  is the distance from target rotating center to radar and  $\theta(t)$  is the rotation angle. The return signal can be expressed as a sum of scattering points responses:

$$s(t) = \sum_{p=1}^K A_p \exp \left\{ -j \frac{4\pi}{\lambda} [R_0 + y_p \cos \theta(t) + x_p \sin \theta(t)] \right\} \quad (2)$$

In (2),  $A_p$  is the complex backscattering coefficient of point  $p$ .  $\lambda$  and  $K$  are the wavelength and number of scattering points, respectively.

The Doppler frequency induced by the rotation from a scattering point can be written as follows:

$$f_d = \frac{2d\theta(t)}{\lambda dt} (x \cos \theta(t) - y \sin \theta(t)) \quad (3)$$

During the imaging observation interval, the rotation angle is small enough and thus can be approximated by the second-order Taylor expansion.

$$\begin{aligned} \cos \theta(t) &\approx 1 - \theta(t)^2 / 2 \\ \sin \theta(t) &\approx \theta(t) \end{aligned} \quad (4)$$

With the assumption that the rotation rate of the target in CPI is  $\omega(t)$ , the Doppler frequency in (3) can be rewritten as:

$$f_d \approx \frac{2\omega(t)}{\lambda} \left( x - \frac{\theta(t)^2}{2} x - y\theta(t) \right) \quad (5)$$

Equation (5) shows that when the target motion is nonstationary, the rotation rate  $\omega(t)$  will be time-varying. As a consequence, the Doppler frequency will be time-varying. Utilizing FT of (2) with

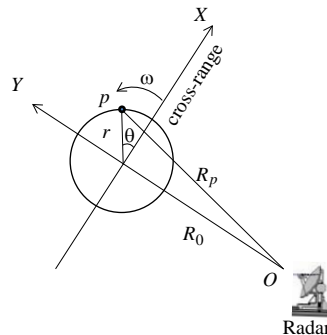


**Figure 1.** Geometry of ISAR imaging.

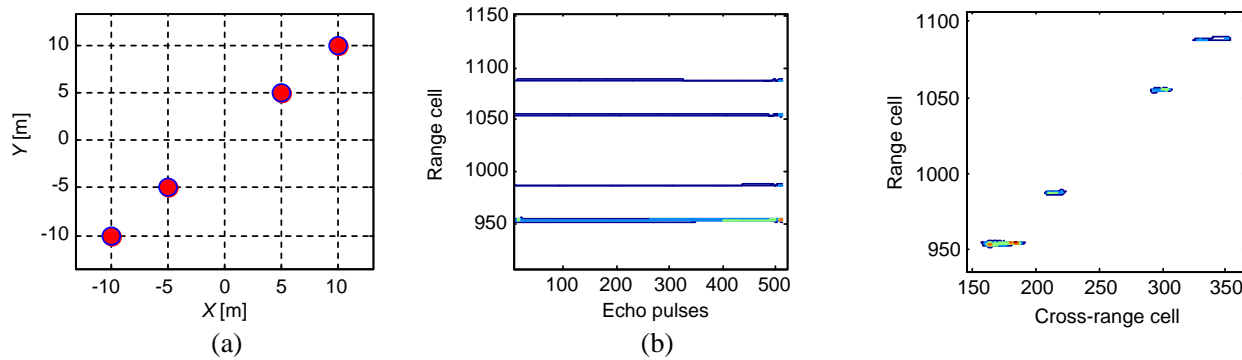


**Figure 2.** Simulated scatterers model 1. (a) Position of scatterers. (b) Range profiles.

respect to  $t$ , the Doppler spectrum will be widened. Therefore, the ISAR image will be blurred in cross-range domain.

As shown in Figure 2(a), a four-point nonuniform rotation model is given to simulate the influence of maneuvering motion. The scattering points are symmetrical to the origin point  $(0, 0)$ . The carrier frequency is  $f_c = 10$  GHz, the bandwidth is  $B = 1$  GHz, and the pulse repetition frequency is  $\text{PRF} = 200$  Hz. The pulse number used for imaging is 512 and the high resolution range profile (HRRP) consists of 2048 range bins.

Suppose that motion compensation techniques are employed to remove the influence of translational motion, thus the model handles pure rotation circumstance. The rotation rate is  $\omega = 0.039$  rad/s and the acceleration of rotation is  $\omega' = 0.009$  rad/s<sup>2</sup>. The range profile corresponding to part of the range bins is shown in Figure 2(b). The RD ISAR image is shown in Figure 3, from which it can be seen that the RD image of the simulated scattering-point model is blurred in the azimuth direction. Therefore, in order to achieve a better-focused ISAR image for the maneuvering target, the RID imaging method based on TF analysis has been widely adopted.

### 3. RANGE INSTANTANEOUS DOPPLER ISAR IMAGING

After compensating the translational motion, the RID ISAR imaging algorithm applies TF analysis to obtain the TF spectrums for each range bin. Subsequently, the instantaneous ISAR image of the target in the azimuth direction can be obtained by taking slices in the slow-time domain. The flow chart of the RID imaging is shown in Figure 4. Considering the echo with pulse number of  $M$  and range bins number of  $N$ , the common RID imaging method can give  $M$  frames of  $N \times M$  RID images.

As previously mentioned, in the traditional RID method, the instantaneous Doppler spectrum lines of different range bins are from the same time slice [15]. However, in practice, the RID image of maneuvering targets may not be the optimal one because the instantaneous Doppler distribution of different range bins will not reach to the optimum at the same time slice.

The TF distribution of the four range bins in Figure 2(b) is given in Figure 5. The TF analysis tool utilized in this study is reassigned Gabor transform [16]. The reassigned Gabor transform reduces or completely removes the cross-terms and diffuses other signal components, and also enhances the TF aggregation of the signals and improves the readability of TF representation [17]. From Figure 5, we can observe that the distribution of the four range bins in TF plane is distinct. Due to the time-varying back-scattering coefficient and range migration of each scattering point, the TF spectrum varies in the slow-time domain. Figure 6 shows the RID images when the time slices are  $t_m = 0$ ,  $t_m = 256$  and  $t_m = 512$ . It can be seen that scattering points of the target may disappear in RID image when the sample time slice is fixed.

Thus the matter of how to choose the time slices during the traditional RID imaging procedure brings uncertain effects to the final results. In the next section, a new RID method based on adaptive Doppler spectrum extraction is proposed to resolve the problem.

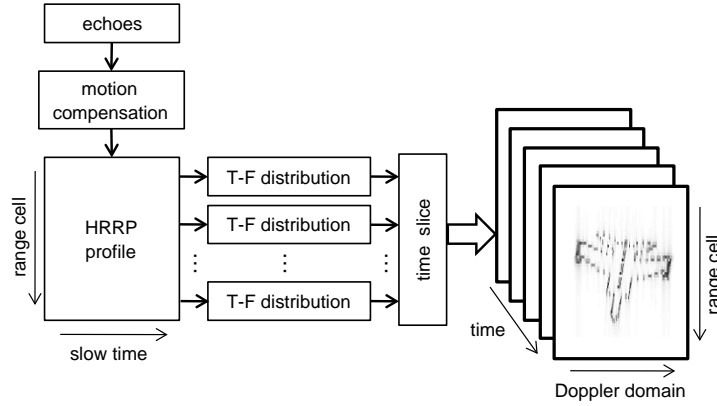


Figure 4. RID image flow chart.

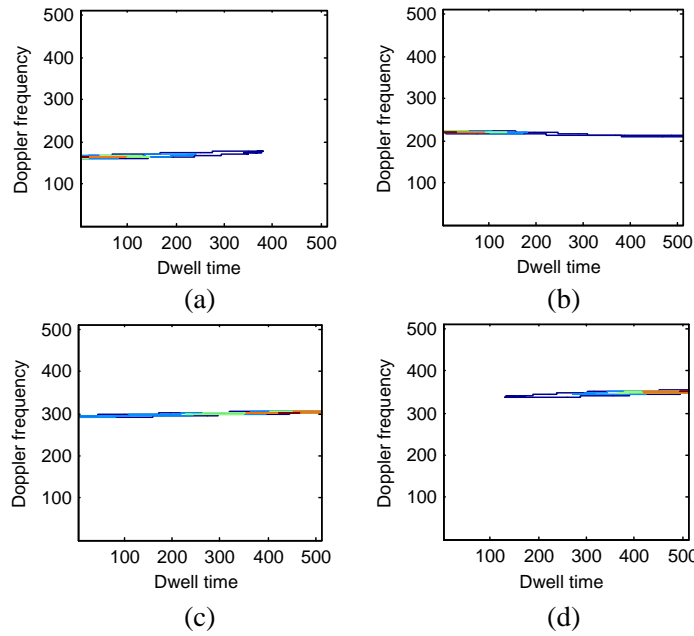


Figure 5. Reassigned Gabor spectrum of four range bins in model 1. (a) T-F spectrogram of range bin 953. (b) T-F spectrogram of range bin 988. (c) T-F spectrogram of range bin 1055. (d) T-F spectrogram of range bin 1089.

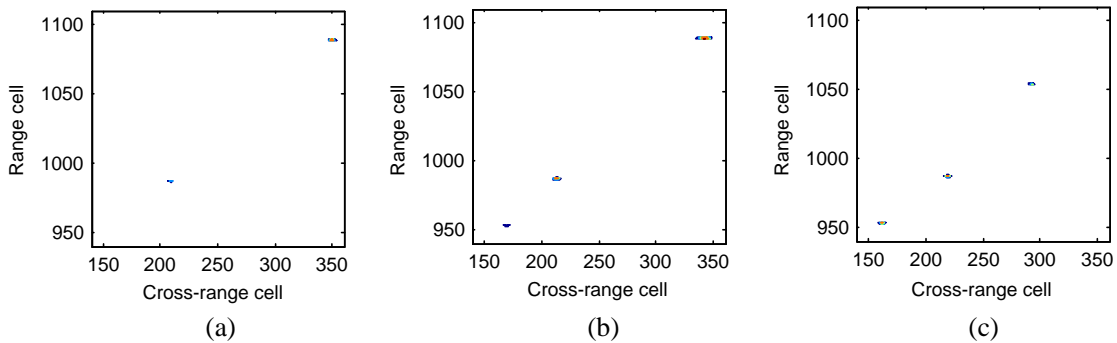


Figure 6. RID images of model 1. (a) Time slice at  $t = 0$ . (b) Time slice at  $t = 256$ . (c) Time slice at  $t = 512$ .

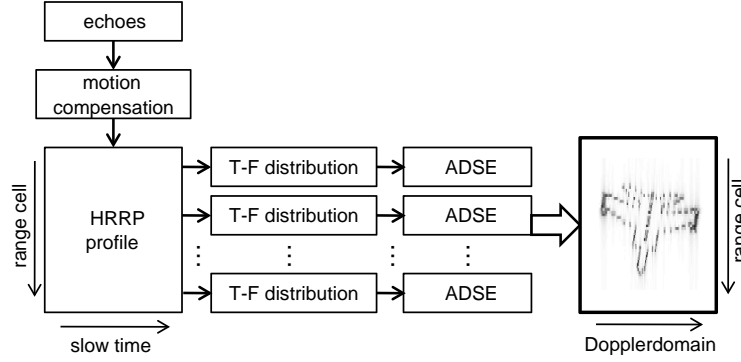


Figure 7. RID imaging flow chart based on adaptive Doppler spectrum extraction.

#### 4. RID IMAGING BASED ON ADAPTIVE DOPPLER SPECTRUM EXTRACTION

From the analysis above, it can be seen that scattering points on the target corresponding to different range bins may disappear when traditional RID imaging method is utilized. To solve this problem, an improved RID imaging algorithm is proposed. The flow chart is illustrated in Figure 7. Distinguished from the traditional RID imaging, the improved method is applied to choose the optimal Doppler spectrum for each range bin after the TF spectrum is obtained. Following that, the obtained optimal Doppler spectrums are combined to achieve a new RID image.

##### 4.1. Evaluation Function of Optimal Doppler Spectrum

The evaluation function for choosing the optimal Doppler spectrum is of great significance. From the analysis above, it can be deduced that the optimal Doppler spectrum requires three criteria to be fulfilled. First, it should contain sufficient cross-range bins; secondly, the energy of the spectrum maintains a concentrate distribution in few cross-range bins; and thirdly, the energy of the optimal spectrum should also be the maximum one. In this section, an evaluation function is designed to characterize the optimal Doppler spectrum numerically.

In ISAR imaging, two most popular standards used to evaluate the sharpness of a distribution function are contrast and entropy [18]. The sharper a distribution function is, the larger its contrast is or the smaller its entropy is.

The TF distribution of a range bin  $G(t, f)$  is normalized in amplitude, and it can be expressed as:

$$G'(t, f) = G(t, f) / \max(G(t, f)) \quad (6)$$

For the instantaneous Doppler spectrum  $G'(t_i, f)$ , which is the slice of normalized TF distribution  $G'(t, f)$  at time  $t_i$ , the contrast is defined as:

$$C(G'(t_i, f)) = \frac{\sigma(|G'(t_i, f)|^2)}{E(|G'(t_i, f)|^2)} \quad (7)$$

where  $\sigma(|G'(t_i, f)|^2)$  is the standard deviation of  $|G'(t_i, f)|^2$  and  $E(|G'(t_i, f)|^2)$  is the mean of  $|G'(t_i, f)|^2$ .

The entropy of  $G'(t_i, f)$  is defined as:

$$H(G'(t_i, f)) = - \sum_{j=1}^M \frac{|G(t_i, f_j)|^2}{S} \ln \frac{|G(t_i, f_j)|^2}{S} \quad (8)$$

where  $S = \sum_{j=1}^M |G'(t_i, f_j)|^2$  is the energy of  $G'(t_i, f)$ .

The question here is whether the contrast and entropy are able to detect the optimal spectrum. Here, we provide an example to illustrate the question. Four simulated Doppler spectrum curves are

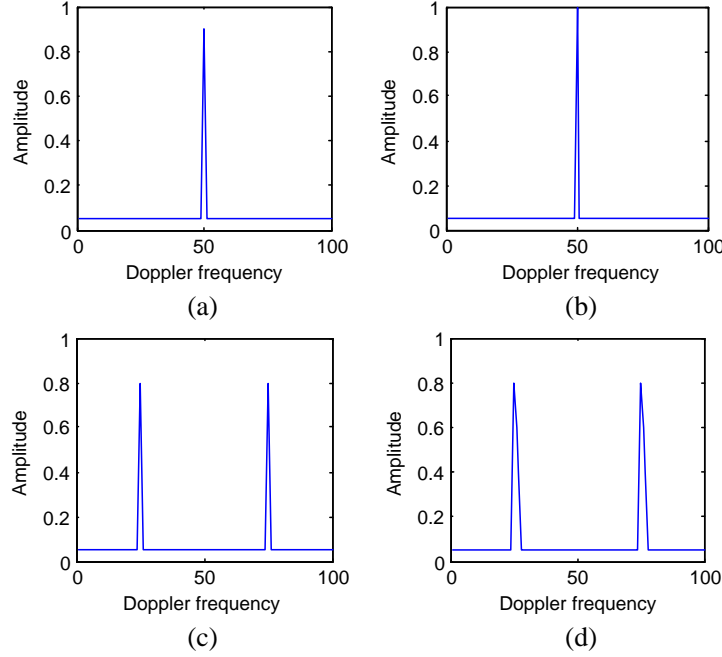


**Figure 8.** Simulated Doppler spectrum. (a) Spectrum *A*. (b) Spectrum *B*. (c) Spectrum *C*. (d) Spectrum *D*.

given in Figure 8. Curves *A* and *B* have one peak in the spectrum, while curves *C* and *D* have two peaks. For comparison, let's suppose that spectrum *C* be better focused than *D*. Based on the definition of optimal Doppler spectrum, it can be easily determined that *C* is the optimal one. The contrast and entropy of the curves are  $C(A) = 0.61$ ,  $C(B) = 0.80$ ,  $C(C) = 0.51$ ,  $C(D) = 0.42$ ,  $H(A) = 14.91$ ,  $H(B) = 14.79$ ,  $H(C) = 15.10$ , and  $H(D) = 15.78$ , respectively. Based on the contrast or entropy, *B* would be erroneously selected as the optimal spectrum, because that contrast and entropy can measure only the sharpness efficiently but the information of peaks number cannot be obtained. In other words, contrast and entropy are not competent for the first criterion of the optimal spectrum. To overcome this shortage, a new measure standard based on gradient energy function is presented.

$$\begin{cases} G(t_{\text{opt}}, f) = \max_{i \in [1, M]} [GradE(G'(t_i, f))] \\ GradE(G'(t_i, f)) = \sum_{j=1}^{M-1} |G'(t_i, f_{j+1}) - G'(t_i, f_j)|^2 \end{cases} \quad (9)$$

In (9),  $GradE(G'(t_i, f))$  is defined as the gradient energy of the distribution function. The GEF can measure the sharpness of the curve and the energy simultaneously [19, 20]. The sharper a distribution function is and the more peaks contains in the distribution function, the larger the gradient energy is. For this reason, the GEF is in accordance with the optimal spectrum standard. By calculating the gradient energy of the four curves, we can get the  $GE(A) = 1.45$ ,  $GE(B) = 1.81$ ,  $GE(C) = 2.25$  and  $GE(D) = 1.53$ . Distinctly, curve *C* is the optimal one. Without loss of generality, the simulation results can be extended to real situations.

## 4.2. Improved RID Imaging Flow

By now, we can sum up the procedure of the newly proposed RID ISAR imaging algorithm as follows.

Step 1: Take translational motion compensation on the HRRPs, including range alignment and phase adjustment. The compensated HRRPs with  $M \times N$  dimensions are obtained, where  $M$  denotes the number of HRRPs and  $N$  is the number of range bins in HRRP.

Step 2: Apply reassigned Gabor transform on the  $n$ th ( $n \in [1, N]$ ) range bin. The normalized TF distribution is indicated as  $G'_n(t, f)$ . It should be noted that, the range bins on the target are normally

part of all range bins. Therefore, scattering centers extraction technique can be used to reduce the range bin number under processing [21].

Step 3: Calculate the gradient energy  $Grid(G'_n(t_i, f))$  of each Doppler spectrum slice in slow-time domain. Following that, select the optimal Doppler spectrum of the  $n$ th range bin according to the GEF.

Step 4: Repeat Step 2 and Step 3 until all of the range bins are scanned.

Step 5: Combine all of the optimal Doppler spectrums to export the final RID image.

### 5. EXPERIMENT AND PERFORMANCE ANALYSIS

In this section, simulated and measured data are used for performance analysis of the proposed RID ISAR imaging method.

#### 5.1. Simulated Data Results

We first give the ISAR image obtained via proposed algorithm of the simulated data in Section 2. The result is shown in Figure 9. It can be seen that the new image in Figure 9 is better focused than that in Figure 3 and more holonomic than the images in Figure 6.

Then the simulated MIG-25 data is used to test the algorithm. The radar transmits stepped-frequency waveform, the carrier frequency is 9 GHz, the bandwidth is 512 MHz, and the pulse repetition frequency is 15000 Hz. The simulated aircraft is composed of 120 scattering points of equal reflectivity. Figure 10(a) shows the ISAR image constructed based on RD algorithm. The blurring effects due to the MTRC are evident. In Figures 10(b), (c) and (d), the three RID images are obtained by taking the slice along the slow-time at unit 1, 256 and 512. Figure 10(e) presents the RID image obtained via the proposed RID imaging method based on entropy function and Figure 10(f) shows the image obtained by new method based on GEF. The results indicate that the proposed algorithm performs better than the traditional RID method. Furthermore, Figures 10(e) and (f) indicate that the evaluation function is significant in the proposed approach.

The image entropy is chosen as the standard to evaluate the performance of each algorithm,  $t$ . The results are shown in Table 1, from which we can see the effectiveness of the propose method.

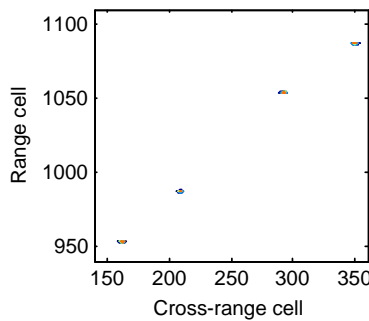
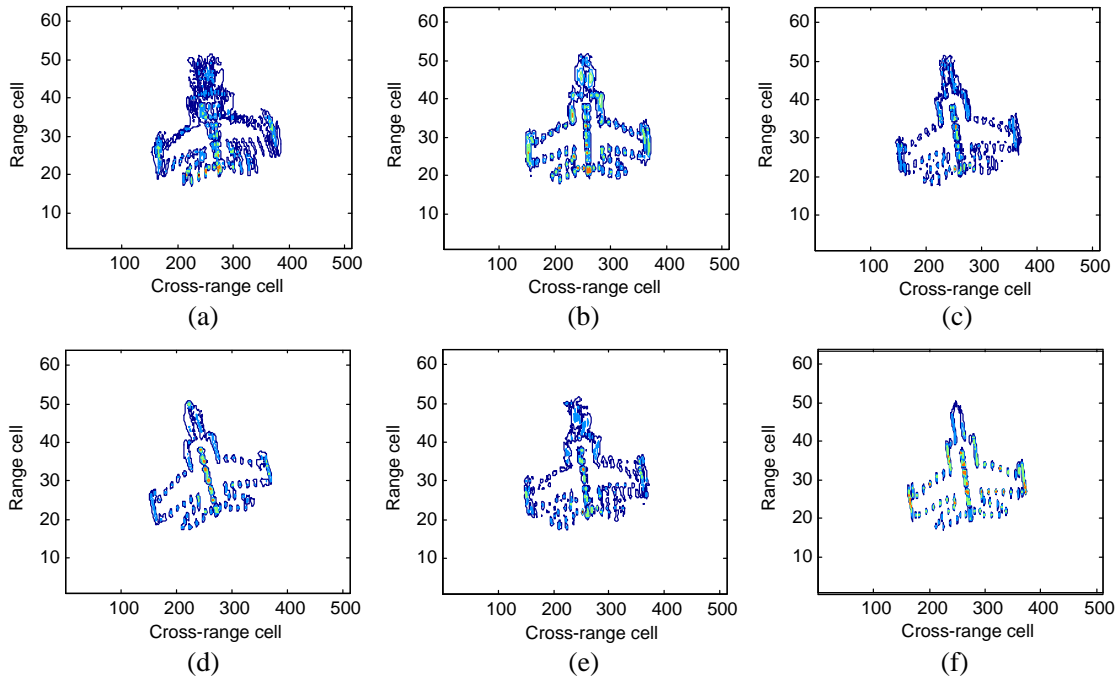


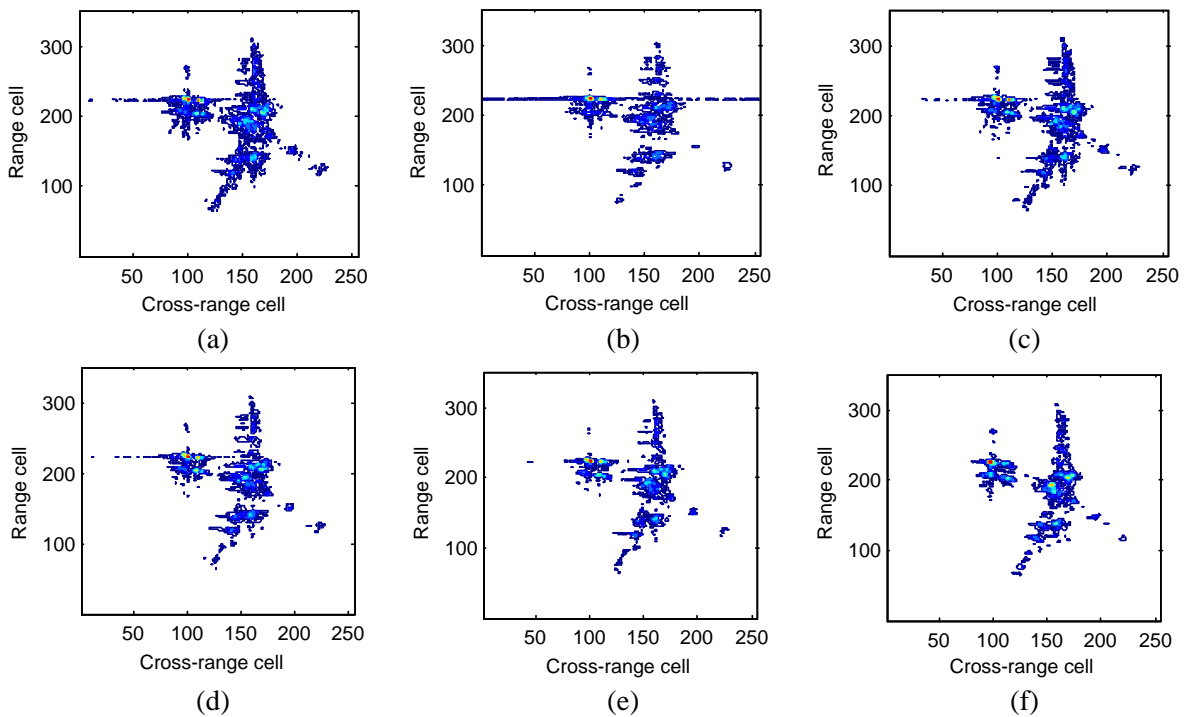
Figure 9. RID image of model via proposed method.

Table 1. The image entropy of different imaging method.

Method	RD imaging	Traditional RID imaging			Proposed RID imaging	
		time unit 1	time unit 256	time unit 512	via entropy function	via GEF
Image entropy	7.8216	7.6261	7.4817	7.3696	7.5825	7.2045



**Figure 10.** ISAR images of MIG-25. (a) RD image. (b) RID image in time unit 1. (c) RID image in time unit 256. (d) RID image in time unit 512. (e) RID image by proposed method via entropy function. (f) RID image by proposed method via GEF.



**Figure 11.** Real measured data ISAR images of Boeing 737. (a) RD image. (b) RID image in time unit 1. (c) RID image in time unit 256. (d) RID image by proposed method via entropy function. (e) RID image by proposed method via contract function. (f) RID image by proposed method via GEF.

**Table 2.** The image entropy of different imaging method.

Method	RD imaging	Proposed RID imaging		Proposed RID imaging		
		time unit 1	time unit 256	via entropy function	via contract function	via GEF
Image entropy	9.3020	7.2501	7.3260	6.7222	6.8799	6.5763
GEF of the 200 range bin		0.5125	0.4007	1.7560	2.1362	2.2582

## 5.2. Real Data Results

Figure 11 presents the ISAR imaging result obtained from field-measured data of Boeing737 in flight. These data were collected by experimental ground-based imaging radar of Science and Technology on Automatic Target Recognition Laboratory (ATR). The carrier frequency is  $f_c = 10$  GHz, the bandwidth is  $B = 1$  GHz and the pulse repetition frequency is  $\text{PRF} = 400$  Hz. The pulse number used for imaging is 256 and the HRRP consists of 350 range bins. During the CPI, the airplane is invariably maneuvering for a certain degree, which leads to ambiguity on cross-range by applying the RD algorithm. Figures 11(b) and (c) show the RID images obtained by taking the slice along the dwelling time at unit 1 and 256. It can be seen that the image quality improves insignificantly. From Figure 11(b), one can note that the quality of the RID image even declines in comparison with the RD image, when the time slice is chosen incorrectly. Figures 11(d) and (e) show the image obtained by the proposed RID flow based on entropy and contrast function. Figure 11(f) shows the image obtained via the proposed RID algorithm, which performs better distinctly. The results indicate that the proposed algorithm performs better than the traditional RID method. Furthermore, Figures 11(d), (e) and (f) also indicate the significance of evaluation function. The image entropy and GEF of a selected range bin for the RID imaging are shown in Table 2. As we can see that the GEF of the proposed method reaches the largest and get the best performance.

## 6. CONCLUSIONS

For maneuvering targets, such as military aircraft, the ISAR image is blurred on cross-range domain when the RD algorithm is applied. RID imaging method is often used to resolve the Doppler ambiguity. In this paper, a new RID ISAR imaging method base on ADSE is proposed. The proposed algorithm first utilizes the reassigned Gabor analysis on each range bin, whose translational motion has been compensated, to obtain the TF distribution. Then, the optimal Doppler spectrums are extracted by using the gradient energy function. Finally, all of the optimal Doppler spectrums are combined to obtain a 2D RID image of the target. The results obtained from simulated and field-measured data verify the superiority of the proposed algorithm.

## ACKNOWLEDGMENT

This work was partly supported by the National Natural Science Foundation of China (No. 61002025).

## REFERENCES

1. Wehner, D. R., *High-resolution Radar*, 2nd Edition, Artech House, Norwood, MA, 1995.
2. Chen, C. C. and H. C. Andrews, "Target motion induced radar imaging," *IEEE Trans. Aerosp. Electron. Syst.*, Vol. 16, No. 1, 2–14, 1980.
3. Park, J. I. and K. T. Kim, "A comparative study on ISAR imaging algorithms for radar target identification," *Progress In Electromagnetics Research*, Vol. 108, 155–175, 2010.

4. Park, S.-H., J.-H. Lee, and K.-T. Kim, "Performance analysis of the scenario-based construction method for real target ISAR recognition," *Progress In Electromagnetics Research*, Vol. 128, 137–151, 2012.
5. Hu, J. M., W. Zhou, and Y. W. Fu, "Uniform rotational motion compensation for ISAR based on phase cancellation," *IEEE Geosci. Remote Sens. Lett.*, Vol. 8, No. 4, 636–640, 2011.
6. Du, L. P. and G. C. Su, "Adaptive inverse synthetic aperture radar imaging for nonuniformly moving targets," *IEEE Geosci. Remote Sens. Lett.*, Vol. 2, No. 3, 247–249, 2005.
7. Wang, Y. and Y. C. Jiang, "ISAR imaging of maneuvering target based on the L-class of fourth-order complex-lag PWVD," *IEEE Trans. Geosci. Remote Sens.*, Vol. 48, No. 3, 1518–1527, 2010.
8. Wang, Y. and Y. C. Jiang, "Inverse synthetic aperture radar imaging of maneuvering target based on the product generalized cubic phase function," *IEEE Geosci. Remote Sens. Lett.*, Vol. 8, No. 5, 958–962, 2011.
9. Berizzi, F., D. Mese, M. Diani, and M. Martorella, "High-resolution ISAR imaging of maneuvering targets by means of the range instantaneous Doppler technique: Modeling and performance analysis," *IEEE Trans. Image Processing*, Vol. 10, No. 12, 1180–1190, 2001.
10. Lv, X. L., M. D. Xing, C. R. Wan, and S. H. Zhang, "ISAR imaging of maneuvering targets based on the range centroid Doppler technique," *IEEE Trans. Image Processing*, Vol. 19, No. 1, 141–153, 2010.
11. Li, J., C. W. Qiu, and L. Zhang, "Time-frequency imaging algorithm for high speed spinning targets in two dimensions," *IET Radar Sonar Navig.*, Vol. 4, No. 6, 806–817, 2010.
12. Thayaparan, T., G. Lampropoulos, S. K. Wong, and E. Riseborough, "Application of adaptive joint time-frequency algorithm for focusing distorted ISAR images from simulation and measured radar data," *IEE Proc. Radar Sonar Navig.*, Vol. 150, No. 4, 213–220, 2003.
13. Muñoz-Ferreras, J. M. and F. Pérez-Martínez, "On the Doppler spreading effect for the range-instantaneous-Doppler technique in inverse synthetic aperture radar imagery," *IEEE Geosci. Remote Sens. Lett.*, Vol. 7, No. 1, 180–184, 2010.
14. Park, J.-H. and N.-H. Myung, "Enhanced and efficient ISAR imaging focusing using the discrete gabor representation in an oversampling scheme," *Progress In Electromagnetics Research*, Vol. 138, 227–244, 2013.
15. Wu, L., X. Z. Wei, H. Q. Wang, and X. Li, "ISAR imaging of targets with complex motion based on discrete chirp Fourier transform for cubic chirps," *IEEE Trans. Geosci. Remote Sens.*, Vol. 50, No. 10, 4201–4212, 2012.
16. Matusiak, E., T. Michaeli, and Y. C. Eldar, "Noninvertible Gabor transforms," *IEEE Trans. Signal Processing*, Vol. 58, No. 5, 2597–2612, 2010.
17. Qian, S. and D. P. Chen, "Discrete Gabor transform," *IEEE Trans. Signal Processing*, Vol. 41, No. 7, 2429–2438, 1993.
18. Wang, J. F. and D. Kasilingam, "Global range alignment for ISAR," *IEEE Trans. Aerosp. Electron. Syst.*, Vol. 39, No. 1, 351–357, 2003.
19. Zhu, J. Y. and N. C. Wang, "Image quality assessment by visual gradient similarity," *IEEE Trans. Image Processing*, Vol. 21, No. 3, 919–933, 2012.
20. Kim, D. O., H. S. Han, and R. H. Park, "Gradient information-based image quality metric," *IEEE Trans. Consumer Electronics*, Vol. 56, No. 2, 930–936, 2010.
21. Kim, K. T. and H. T. Kim, "One-dimensional scattering centre extraction for efficient radar target classification," *IEE Proc. Radar Sonar Navig.*, Vol. 146, No. 3, 147–158, 1999.